



Contents lists available at ScienceDirect

Earth and Planetary Science Letters

journal homepage: www.elsevier.com/locate/epsl

Full waveform tomography for radially anisotropic structure: New insights into present and past states of the Australasian upper mantle

Andreas Fichtner^{a,c,*}, Brian L.N. Kennett^b, Heiner Igel^a, Hans-Peter Bunge^a^a Department of Earth and Environmental Sciences, Ludwig Maximilian University, Theresienstrasse 41, 80333 Munich, Germany^b Research School of Earth Sciences, The Australian National University, Bldg 61 Mills Road, Acton ACT, 0200 Australia^c Department of Earth Sciences, Utrecht University, Budapestlaan 4, 3584 CD Utrecht, The Netherlands

ARTICLE INFO

Article history:

Received 4 September 2009

Received in revised form 23 November 2009

Accepted 4 December 2009

Available online xxx

Edited: L. Stixrude

Keywords:

seismic waveform inversion

spectral-element method

adjoint method

seismic anisotropy

lattice-preferred orientation

Australia

ABSTRACT

We combine spectral-element simulations and adjoint techniques in a non-linear full seismic waveform tomography for the radially anisotropic structure of the Australasian upper mantle. Our method allows us to explain 30 s waveforms in detail, and it yields tomographic images with locally 2° lateral resolution. In the course of 19 conjugate-gradient iterations the total number of exploitable waveforms increased from 2200 to nearly 3000. The final model, AMSAN.19, thus explains data that were not initially included in the inversion. This is strong evidence for the effectiveness of the inversion scheme and the physical consistency of the tomographic model.

AMSAN.19 confirms long-wavelength heterogeneities found in previous studies, and it allows us to draw the following inferences concerning the past and present states of the Australian upper mantle and the formation of seismic anisotropy: (1) Small-scale neutral to low-velocity patches beneath central Australia are likely to be related to localised Paleozoic intraplate deformation. (2) Increasing seismic velocities between the Moho and 150 km depth are found beneath parts of Proterozoic Australia, suggesting thermochemical variations related to the formation and fragmentation of a Centralian Superbasin. (3) Radial anisotropy above 150 km depth reveals a clear ocean–continent dichotomy: We find strong $v_{sh} > v_{sv}$ beneath the Coral and Tasman Seas. The anisotropy is strongest at the top of the inferred asthenospheric flow channel, where strain is expected to be largest. Radial anisotropy beneath the continent is weaker but more variable. Localised patches with $v_{sh} < v_{sv}$ appear, in accord with small-scale intraplate deformation. (4) The ocean–continent dichotomy disappears gradually between 150 and 250 km depth, where the continental lithospheric mantle and the oceanic asthenosphere pass into the underlying convecting mantle. (5) Significant anisotropy exists below 250 km depth. Its character can be explained by sublithospheric small-scale convection and a change in the dominant glide system of olivine.

© 2009 Elsevier B.V. All rights reserved.

1. Introduction

Recent progress in numerical methods and computer science allows us today to simulate the propagation of seismic waves through realistically heterogeneous Earth models with unprecedented accuracy (e.g. Faccioli et al., 1997; Komatitsch and Tromp, 2002; Dumbser and Käser, 2006). These new capabilities must now be used to further our understanding of the Earth's structure and dynamics.

Full waveform tomography is a tomographic technique that takes advantage of numerical solutions of the elastic wave equation (e.g. Konishi et al., 2009; Tape et al., 2009; Fichtner et al., 2009a,b). Numerically

computed seismograms automatically contain the full seismic wavefield, including all body and surface wave phases as well as scattered waves generated by lateral variations of the model Earth properties. The amount of exploitable information is thus significantly larger than in tomographic methods that are based, for example, on measurements of surface wave dispersion or the arrival times of specific seismic phases. The accuracy of the numerical solutions and the exploitation of complete waveform information result in tomographic images that are both more realistic and better resolved (Fichtner et al., 2009b; Tape et al., 2009).

Here, we present a full waveform tomography for the radially anisotropic structure of the upper mantle in the Australasian region. Our method allows us to explain the details of seismic waveforms with periods between 30 s and 200 s, and it provides tomographic images with locally 2° lateral resolution. The tomograms provide new insight into the structure and dynamics of the Australasian upper mantle and the formation of seismic anisotropy.

This paper is organised as follows: we start with a condensed description of our full waveform tomographic method and its principal

* Corresponding author. Department of Earth and Environmental Sciences, Ludwig Maximilian University, Theresienstrasse 41, 80333 Munich, Germany. Tel.: +49 89 21804226.

E-mail addresses: fichtner@geophysik.uni-muenchen.de (A. Fichtner), brian.kennett@anu.edu.au (B.L.N. Kennett), igel@geophysik.uni-muenchen.de (H. Igel), bunge@lmu.de (H.-P. Bunge).

advantages. This is followed by the details of the data selection and processing. We then present our 3D radially anisotropic model of the Australasian region. Subsequently we discuss the achieved waveform fit and the relation to previous tomographic models. In the discussion section we interpret both the isotropic and the anisotropic structure in terms of the past and present states of the Australasian upper mantle. Separate SH and SV velocity models, resolution tests and spatially filtered tomographic images are presented in the electronic supplement.

2. The full waveform tomographic method

2.1. Numerical waveform modelling

A defining property of full waveform tomography is the purely numerical solution of the elastic wave equation, that does not suffer from the restrictions of ray theory or truncated normal mode summations. Numerical solutions of the wave equation accurately account for the complete physics of seismic wave propagation through realistically heterogeneous Earth models. The observed waveform misfits thus result from undiscovered Earth structure and not from approximation errors, that may otherwise distort the tomographic images.

We implemented a spectral-element method to solve the elastic wave equation in an Earth model with 3D variations of the elastic and anelastic parameters (Fichtner et al., 2009a). The discrete equations are solved in parallel on 126 processors (Oeser et al., 2006). As crustal model we use a long-wavelength equivalent version of crust2.0 (Bassin et al., 2000). Its construction is described in Fichtner and Igel (2008), and Fichtner et al. (2009a).

2.2. Measurement of full waveform misfit

The resolution of tomographic images depends on the amount of data that enters the inversion process. To extract as much waveform information as possible, we measure time–frequency phase misfits (Fichtner et al., 2008). They quantify the phase differences between observed and synthetic waveforms at different times and for a continuous range of frequencies (5 mHz to 35 mHz). The principal advantages of the time–frequency phase misfit are (1) a quasi-linear relation to 3D Earth structure, (2) applicability to all types of seismic waves, including interfering phases that are commonly observed at regional distances, and (3) independence from absolute amplitudes that are strongly influenced by shallow structures such as sedimentary basins.

2.3. Model parameterisation

Our elastic model is parameterised in terms of density, ρ , the wave speeds of vertically and horizontally polarised S waves, v_{sv} and v_{sh} , the wave speeds of horizontally and vertically travelling P waves, v_{ph} and v_{pv} , and the parameter η described in detail by Takeuchi and Saito (1972). The data used in this study are mostly sensitive to variations in v_{sv} and v_{sh} . Sensitivity with respect to v_{ph} and v_{pv} is small, and sensitivity with respect to ρ and η is negligible. This implies that v_{ph} , v_{pv} , ρ and η can hardly be resolved. Therefore, following Nettles and Dziewonski (2008), we set the variations of v_{ph} and v_{pv} to 0.5 times the variations of v_{sh} and v_{sv} . We furthermore disregard lateral variations in ρ and set $\eta = 1$, consistent with the isotropic initial model (Fig. 1). The restrictions imposed on the variations of the parameters ρ , η , v_{ph} and v_{pv} are to some degree subjective. Their small sensitivities, however, ensure that they have a negligible influence on the lateral variations of v_{sh} and v_{sv} (Nettles and Dziewonski, 2008).

As basis functions we use blocks that extend $1^\circ \times 1^\circ$ laterally and 10 km vertically. This parameterisation is chosen such that structures that we expect to be resolvable can be represented with sufficient

accuracy. The expected resolution lengths are 2° to 5° laterally and 20 km to 50 km vertically. This estimate is based on previous tomographies where similar amounts of data were used (e.g. Debayle and Kennett, 2000a; Fishwick et al., 2005).

Our parameterisation does not include azimuthal anisotropy because the limited data coverage (Fig. 2) does not allow us to simultaneously determine source locations and azimuthal wave speed variations. Moreover, azimuthal anisotropy involves too many unconstrainable elastic parameters, that would, however, be required for iterative improvement of the tomographic models.

2.4. Misfit minimisation and initial models

We iteratively minimise the cumulative phase misfit using a pre-conditioned conjugate-gradient method (Fichtner et al., 2009b). The gradients of the phase misfit with respect to v_{sh} and v_{sv} are computed via the adjoint method (e.g. Tarantola, 1988; Tromp et al., 2005; Fichtner et al., 2006; Sieminski et al., 2007a,b).

To ensure the fast convergence of the iterative inversion, we implement a 3D initial model that contains the long-wavelength features of the Australasian upper mantle. For both the initial SH and SV wave speeds we use a smoothed version of the model by Fishwick et al. (2005). We set the initial P wave speed variations to 0.5 times the initial S wave speed variations. This is consistent with results from refracted body wave studies (Kaiho and Kennett, 2000). As elastic 1D reference model we use the isotropic version of PREM (Dziewonski and Anderson, 1981) with the 220 km discontinuity replaced by a gradient, to avoid biases in the 3D tomographic images. We display the elastic 1D reference and 3D initial models in the left panels of Fig. 1.

To minimise the effect of undiscovered 3D anelastic structure on the tomographic images, we implement a 3D model of shear wave attenuation (Abdulah, 2007), shown in the right panels of Fig. 1. It features a weakly attenuative continental lithosphere, strong attenuation beneath the Coral Sea and a pronounced low-attenuation zone between 220 km and 340 km depth. We disregard 3D variations of P wave attenuation because their influence on long-period seismograms is negligible.

3. Data selection and processing

Our data set comprises 2137, three-component recordings from 57 earthquakes that occurred in the Australasian region between 1993 and 2009. The estimated signal-to-noise ratio in the period range from 30s to 150s exceeds 15. A maximum event magnitude of $M_s = 6.9$ allows us to neglect finite-source effects. About 80% of the data were recorded at permanent stations operated by Geoscience Australia, IRIS and GEOSCOPE. The remaining 20% originate from the SKIPPY, KIMBA, QUOLL and TASMAL experiments, undertaken by the Australian National University.

From the observed seismograms we manually select waveforms that show a clear correspondence to synthetic waveforms. Fundamental-mode surface waves account for nearly 60% of the selected waveforms. The remaining 40% are body S waves and higher-mode surface waves. A small fraction of the waveforms is not clearly identifiable. The ray coverage (Fig. 2), is good throughout the eastern part of the continent and decreases towards the west.

Our data set differs from those used in previous surface wave studies (e.g. Zielhuis and van der Hilst, 1996; Simons et al., 1999, 2002; Debayle and Kennett, 2000a; Yoshizawa and Kennett, 2004; Fishwick et al., 2005) in that it contains mostly recordings from permanent stations, many of which were not operational prior to 2006. The improved permanent station coverage allows us to invert a comparatively large number of waveforms with dominant periods > 60s.

For the first iteration, all data are band-pass filtered between 150s and 300s. In the course of the inversion we successively decrease

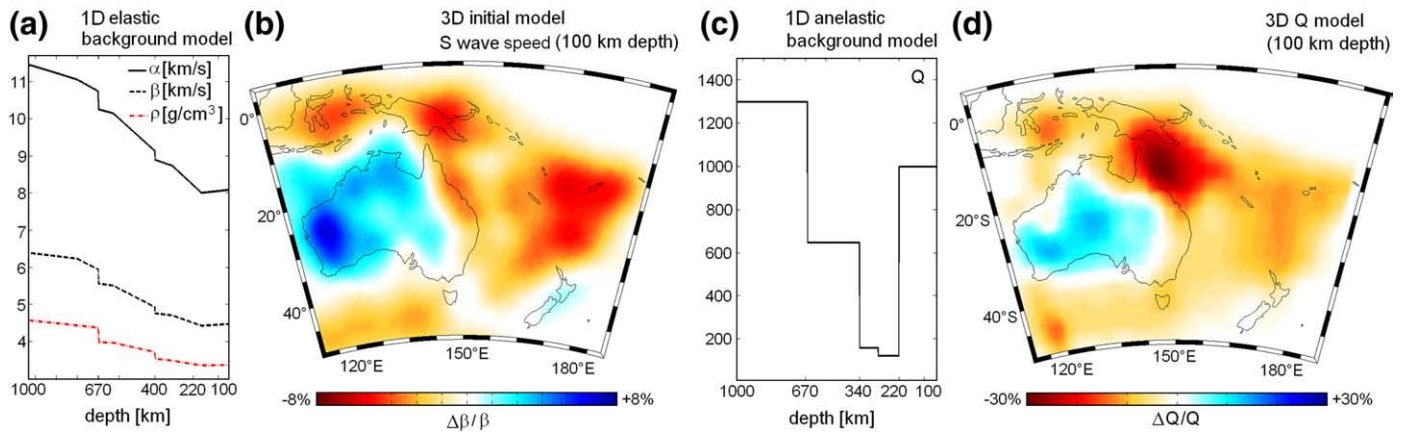


Fig. 1. Left panels: (a) 1D elastic background model of the P wave speed, α , the S wave speed, β , and density, ρ . (b) Horizontal slice at 100 km depth through the initial 3D S wave speed model. Right panels: (c) 1D background model of shear attenuation. (d) Horizontal slice at 100 km depth through the 3D shear attenuation model. The anelastic model does not change during the waveform inversion. 3D variations of P wave attenuation are not included.

the lower cutoff period to 30s. This procedure ensures that the quasi-linearity of the waveform misfit with respect to Earth model perturbations is maintained.

4. Results

4.1. 3D tomographic model

Using the method and the data described in Sections 2 and 3, we inverted for the radially anisotropic upper-mantle structure in the Australasian region. The inversion procedure terminated as the decrease of the cumulative phase misfit from one iteration to the next dropped below 5%. This was the case after 19 iterations. The threshold of 5% was chosen to prevent overfitting the data. The resulting 3D model, AMSAN.19, is presented in Figs. 3 and 4, where we show horizontal slices through the isotropic S wave speed, $v_s^{iso} = 2v_{sh}/3 + v_{sv}/3$, and the radial anisotropy, $(v_{sh} - v_{sv})/v_s^{iso}$. We defer a detailed discussion of the tomographic images to Section 5. In the electronic supplement we present separate images of the SH and SV velocity models and spatially filtered versions of the tomographic images that may aid in the identification of different heterogeneity length scales.

A description of resolution tests can also be found in the electronic supplement. For most of central and eastern Australia and the adjacent Tasman and Coral Seas we estimate that the resolution lengths are around 3° laterally and 40 km vertically, above 200 km depth. Below 200 km depth the estimated resolution lengths are around 7° laterally and 60 km vertically.

A sufficiently large number of iterations are essential to obtain images that are stable in the sense that they do not change much

when additional iterations are performed. The 19th iteration modifies the SH and SV models by less than 0.1% of the reference isotropic S wave speed. However, the changes are mostly above 0.5% during the first 12 iterations. Differences between the SH and SV models after one iteration and after 19 iterations locally exceed 6%. Iterative changes in the anisotropy are nearly as large.

4.2. Waveform fit

Examples of the final waveform fit are displayed in Fig. 5 for a variety of source–receiver geometries. An extended collection of waveforms and an overview of the misfit statistics are shown in the electronic supplement. Model AMSAN.19 explains the waveforms of the major seismic phases, including higher- and fundamental-mode surface waves and long-period body waves. The fit is good for periods above and including 30 s, where the influence of crustal scattering is small. We point out that complete waveforms – and not only aspects of them, such as dispersion curves – can be modelled accurately.

AMSAN.19 provides a fit of relative amplitudes that is significantly better than for the initial model, even though no information on absolute amplitudes was used in the inversion. This observation suggests (1) that lateral contrasts are imaged accurately and (2) that the time–frequency phase and amplitude misfits are rather strongly related, in agreement with recent results by Tian et al. (2009).

In the course of the iteration, the synthetic waveforms become increasingly similar to the observed waveforms. This allows us to successively include waveforms that were initially not usable due to excessive dissimilarities between data and synthetics. The total number of exploited waveforms increases from about 2200 in the first iteration to nearly 3000 in iteration 19. The final model can thus explain data that have initially not been included in the inversion. This is strong evidence for the effectiveness of the inversion scheme and the physical consistency of the tomographic model.

4.3. Comparison with previous models

Previous efforts to image the Australasian upper-mantle structure include the studies of Zielhuis and van der Hilst (1996), Simons et al. (1999, 2002), Debayle and Kennett (2000a,b), Yoshizawa and Kennett (2004) and Fishwick et al. (2005). While earlier models were essentially based on data from temporary arrays, we mostly use recordings from permanent stations with a broader instrument response that were not operational prior to 2006. The positive effects of using permanent stations are the improved overall data quality, the increased coverage in western Australia and the possibility to exploit a larger number of waveforms with periods above 60s. In contrast

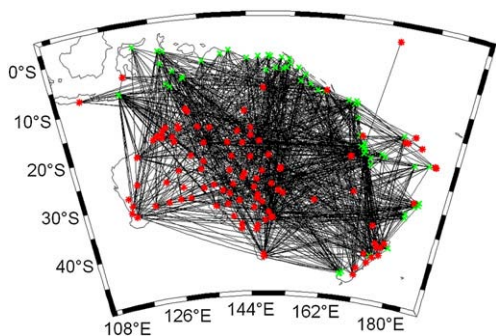


Fig. 2. Ray coverage. Epicentres are plotted as green crosses and stations as red stars. (For interpretation of the references to colour in this figure legend, the reader is referred to the web version of this article.)

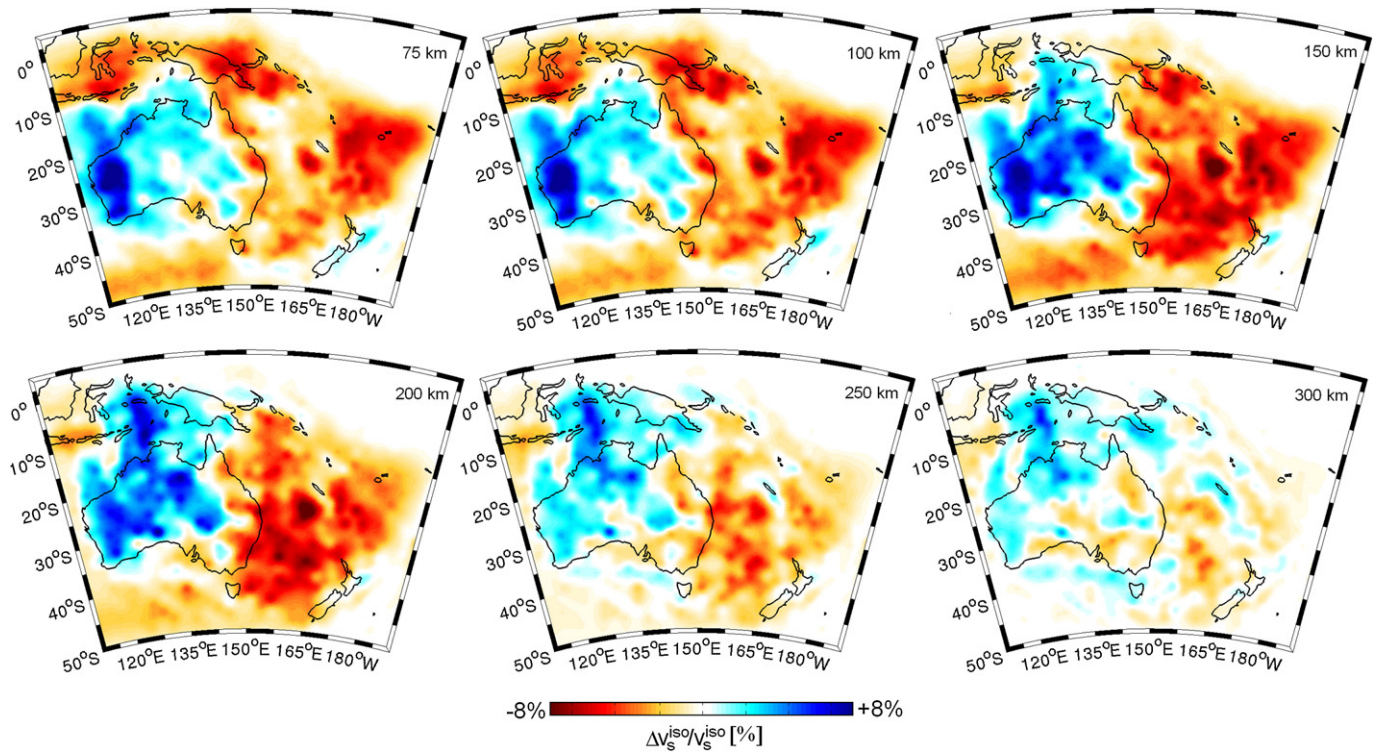


Fig. 3. Horizontal slices through the relative lateral variations of the isotropic S wave speed, $v_s^{\text{iso}} = 2v_{\text{sh}}/3 + v_{\text{sv}}/3$.

to earlier studies, we use all types of seismic waves, including long-period body waves and multiple surface reflections. This improves the resolution especially below 200 km depth. Most previous models were derived from vertical-component data, the only exception being the one by Debayle and Kennett (2000b). The number of recordings

is similar in all studies, ranging from around 1000 to nearly 2300 (Debayle and Kennett, 2000a,b; Simons et al., 2002; Fishwick et al., 2005).

Methodological differences concern all aspects of seismic tomography. In full waveform tomography, we solve the elastic wave

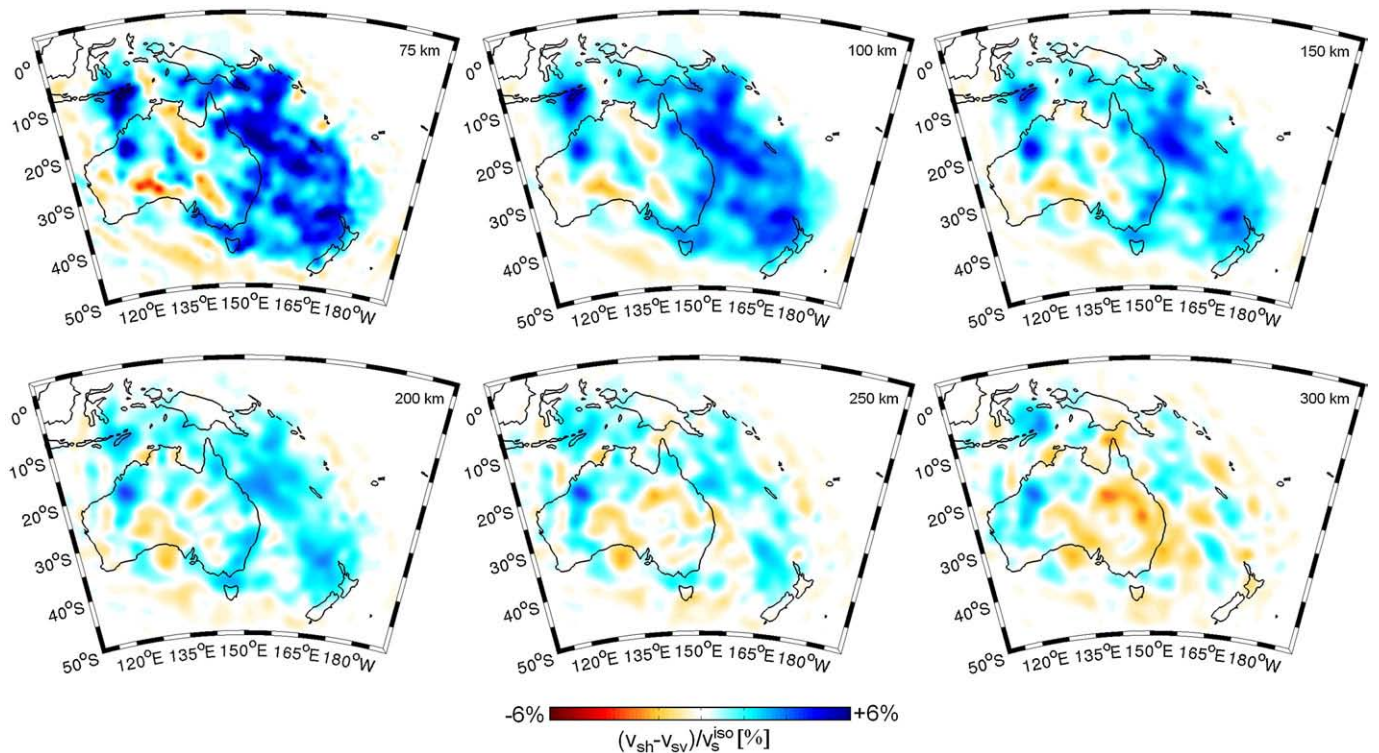


Fig. 4. Horizontal slices through the lateral variations of the anisotropy, $(v_{\text{sh}} - v_{\text{sv}})/v_s^{\text{iso}}$.

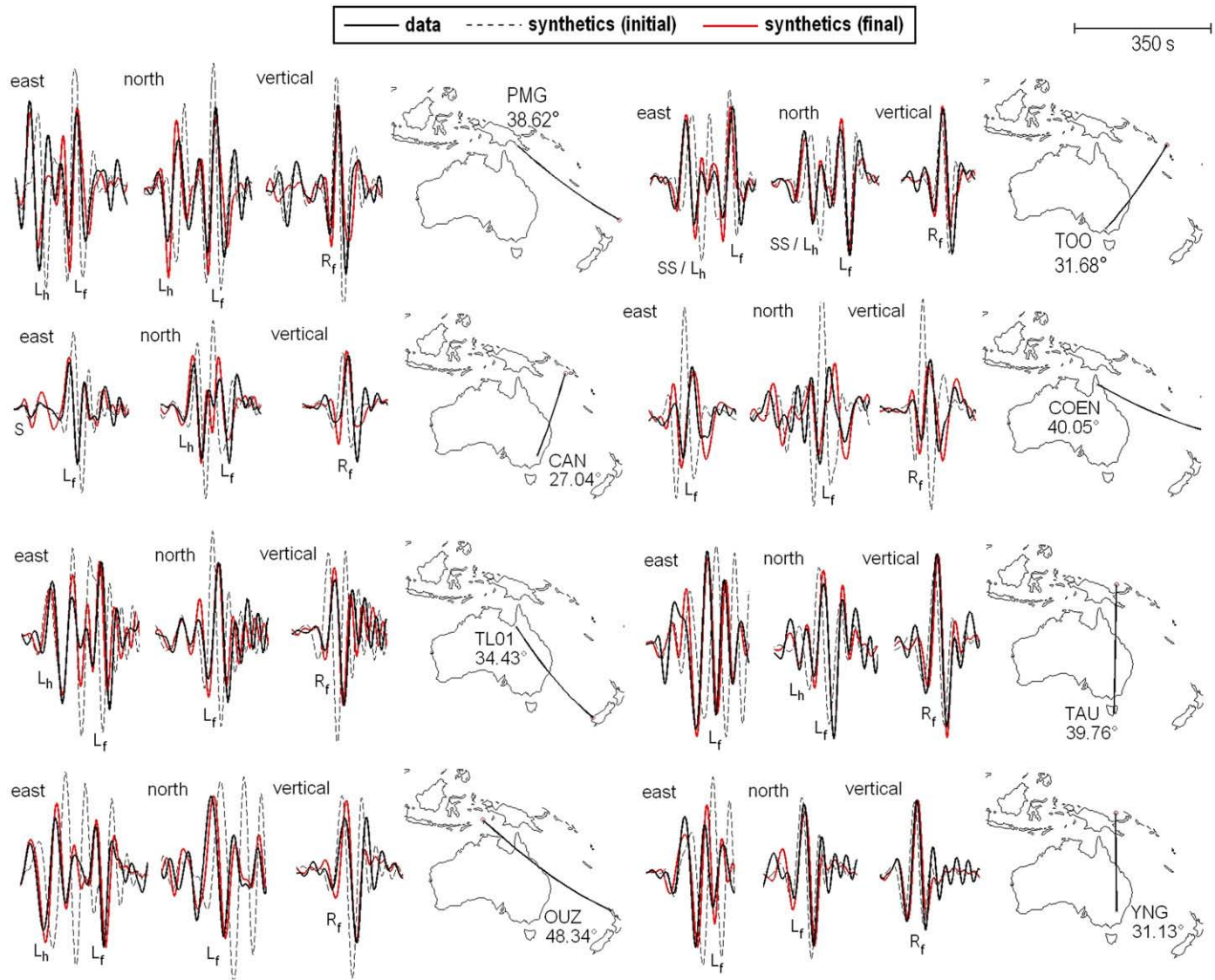


Fig. 5. Exemplary waveform comparisons for a variety of source–receiver geometries. Black solid lines are data, black dashed lines are synthetics for the initial model (Fig. 1) and red solid lines are synthetics for the final model (Figs. 3 and 4). The dominant period is 30 s. A time scale is plotted in the upper-right corner. Identifiable phases are marked for reference ($L_{f/h}$ = fundamental/higher-mode Love wave, $R_{f/h}$ = fundamental/higher-mode Rayleigh wave, SS = surface-reflected S wave). While significant discrepancies exist between data and the initial synthetics, the final synthetics accurately explain both the phases and the amplitudes of the observations.

equation numerically for Earth models with realistically large 3D heterogeneities. This constitutes a major improvement with respect to earlier tomographies where the wave equation was solved using either 1D Earth models or approximations such as ray theory. The numerical solutions allow us (1) to use 3D initial models, (2) to improve the tomographic images iteratively, (3) to exploit complete waveforms and (4) to include data that are not identifiable in terms of the classical seismic phases.

With the exception of the work by Yoshizawa and Kennett (2004), all previous tomographies of the Australasian region worked under the simplifying assumption that sensitivity is spread along a ray. A further improvement of full waveform tomography is thus the computation of 3D sensitivity kernels based on adjoint techniques (e.g. Tarantola, 1988; Tromp et al., 2005; Fichtner et al., 2006). The kernels correctly account for all propagation effects of finite-frequency waves in a 3D heterogeneous Earth. This leads to an improved resolution of the tomographic images (e.g. Yoshizawa and Kennett, 2004; Peter et al., 2009).

On length scales larger than about 1000 km and above 200 km depth, our results for the SV velocity variations, agree well with most SV models found previously. The long-wavelength heterogeneities reflect the thermochemical differences between the major elements of the Australasian upper mantle that we will discuss further in Section 5.

A tomographic study of the radial anisotropy in the Australasian region was performed by Debayle and Kennett (2000a,b). Global studies of radial anisotropy include those of Montagner (2002), Panning and Romanowicz (2006) and Nettles and Dziewonski (2008). Below 100 km depth, the amplitude and the geometry of the long-wavelength anisotropy in AMSAN.19 are most similar to the model of Nettles and Dziewonski (2008). At depths of 100–200 km, the anisotropy is largest under the Coral and Tasman Seas, with a clear $v_{sh} > v_{sv}$ signature. Its strength decreases with depth, and it becomes comparable to the anisotropy under the continent around 230 km. While the anisotropy under the Coral and Tasman Seas is positive above 250 km, it is locally negative under Precambrian Australia.

The setup of our inversion and the approach of Nettles and Dziewonski (2008) share several aspects: The models are parameterised in terms of v_{sh} and v_{sv} , the crustal models are variants of crust2.0 (Bassin et al., 2000), the 1D reference models are isotropic versions of PREM without the 220 km discontinuity and the tomographic model is improved iteratively. We thus conjecture that long-wavelength discrepancies between the anisotropy of AMSAN.19, the regional model of Debayle and Kennett (2000a,b) and the global models of Montagner (2002) and Panning and Romanowicz (2006) are to a large degree the result of methodological differences.

Bozdag and Trampert (2008) demonstrated that crustal corrections influence the inferred upper mantle anisotropy. Previous studies computed crustal corrections from either crust2.0 (Bassin et al., 2000; Panning and Romanowicz, 2006; Nettles and Dziewonski, 2008) or 3SMAC (Nataf and Ricard, 1995; Debayle and Kennett, 2000a, b; Montagner, 2002). Full Waveform Tomography, however, does not require crustal corrections. This is because numerical solutions of the elastic wave equation are accurate also in the presence of a laterally varying crust. The different treatment of the crust is a likely explanation for the differences between AMSAN.19 and the model of Nettles and Dziewonski (2008) around 75 km depth.

Iterative improvement strongly affects radial anisotropy. Its amplitude tends to decrease with a growing number of iterations. Apparent anisotropy is thus increasingly well explained by isotropic structure as the inversion proceeds. This effect, also noted by Nettles and Dziewonski (2008), highlights the non-linearity of the tomographic problem. We hypothesise that non-linearity may partly explain the large anisotropy found by Debayle and Kennett (2000a,b).

Further methodological contributions to long-wavelength differences of the tomographically inferred radial anisotropy include the choices of the initial model and the parameterisation. The neglect of azimuthal

anisotropy may result in discrepancies, where azimuthal coverage is poor. The influence of these factors requires further research, and the different approaches taken in this and previous studies, can all be justified.

5. Discussion

To facilitate the interpretation of the tomographic images, we display a map of the principal surface-geologic features of the Australasian region in Fig. 6. Unless stated otherwise, we will refer to the relative difference between the SH and SV wave speeds, $(v_{sh} - v_{sv})/v_s^{iso}$, simply as anisotropy. Thus, positive anisotropy implies $v_{sh} > v_{sv}$, and negative anisotropy means $v_{sv} > v_{sh}$.

5.1. Isotropic S velocity structure

5.1.1. General features

Our model of the isotropic S wave speed (Fig. 3) confirms the major geologic inferences drawn from earlier SV models (e.g. Zielhuis and van der Hilst, 1996; Simons et al., 1999; Debayle and Kennett, 2000a; Fishwick et al., 2005). We briefly summarise these inferences without further interpretation and then focus on features that have received less attention: (1) The Coral and Tasman Seas are characterised by a pronounced low-velocity zone, centred around 140 km depth. A similar low-velocity zone is not present under continental Australia. (2) A low-velocity band extends along the eastern continental margin down to at least 200 km depth. (3) The seismological sub-continental lithospheric mantle is confined to depths above ≈ 250 km, where the velocity perturbations exceed 5%. (4) The Tasman Line, separating Precambrian from Phanerozoic Australia, is mostly located west of the transition from low to fast wave speeds in the uppermost mantle. (5) A region of high wave speeds under the Arafura and Timor Seas is evidence for a northward continuation of the North Australian craton.

5.1.2. Localised slow wavespeeds beneath Proterozoic Australia

AMSAN.19 reveals localised zero to slightly negative velocity perturbations down to 120 km depth under Proterozoic central Australia, in agreement with Fishwick and Reading (2008) who used AK135 (Kennett et al., 1995) as 1D reference. The nearly zero velocity perturbations are in contrast to the elevated velocities beneath other Proterozoic units such

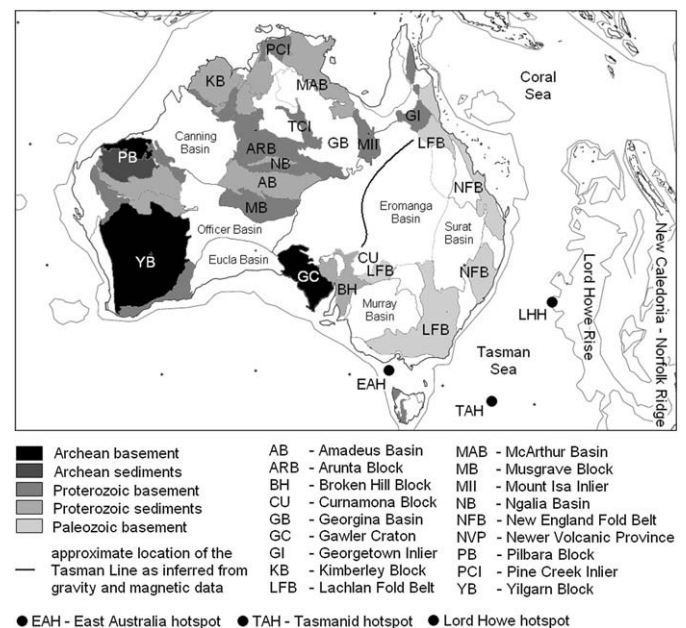


Fig. 6. Map of major geologic feature in the study area, adapted from Myers et al. (1996). Present hotspot locations, indicated by filled circles, are from McDougall and Duncan (1988).

as the Kimberley Block and the MacArthur Basin. Their location directly under the Amadeus Basin suggests a relation to the most recent tectonic events in that region: the intraplate Petermann (550–535 Ma) and Alice Springs (400–300 Ma) orogenies. The resulting uplifts of the Musgrave and Arunta Blocks by several tens of kilometres (e.g. Sandiford and Hand, 1998) may have lead to thermochemical variations in the uppermost mantle that are responsible for seismic velocities that are lower than the Proterozoic average of around +5%.

5.1.3. S velocity increase in the upper lithospheric mantle

In our model we find increasing S velocities between the Moho and 150 km depth in continental Australia and along the convergent margins extending from the Banda Arc to the San Cristobal Trench (Fig. 7). This observation is particularly intriguing in continental Australia. There, the positive velocity gradients are located where the North, South and West Australian cratons amalgamated in the Mesoproterozoic and where a Centralian Superbasin existed between 1000 and 750 Ma (Myers et al., 1996). Positive velocity gradients are, however, weak or absent in the Kimberley, Yilgarn and Pilbara cratons.

Increasing velocities were found in previous studies (e.g. Paulssen, 1987; Levshin et al., 2007; Lebedev et al., 2009). They are, however, not expected in a continental lithospheric mantle with approximately constant composition, where continuously rising temperatures imply decreasing seismic velocities. There are two plausible contributions to the positive velocity gradient: (1) Hales (1969) associated a velocity

jump around 80 km depth under the central United States – the Hales discontinuity – with the transition from spinel to garnet peridotite. Klemme (2004) demonstrated that the presence of Cr causes the spinel–garnet transition to be diffused and shifted to greater depth. The velocity profiles in Fig. 7 are consistent with a spinel–garnet transition around 110 ± 20 km, but limited depth resolution precludes a precise determination of its sharpness. Exceptionally high Cr contents, evidenced by western Australian xenoliths (Jaques et al., 1990), may be responsible for diffuse or absent positive velocity gradients beneath the Yilgarn, Pilbara and Kimberley cratons. (2) Sedimentation and intraplate deformation of the Centralian Superbasin and its later fragments led to a redistribution of heat-producing elements, mostly K, Th and U. The resulting temperature perturbations at depths around the Moho (e.g. Cull and Conley, 1983; Sandiford and Hand, 1998) may also contribute to the anomalous S velocity profiles beneath much of Proterozoic Australia. At 100 km depth, regions with positive velocity gradients exhibit S wave speeds that are on average 3.5% lower than in the Yilgarn, Pilbara and Kimberley cratons. This implies temperatures that are at most 250°C (Goes et al., 2005; Cammarano et al., 2003) higher, which is within a physically plausible range.

The clear association between positive velocity gradients below the Moho and the location of the Centralian Superbasin suggests that lateral variations of velocity gradients in the upper continental lithosphere may be used in future studies as additional constraints on its thermochemical state.

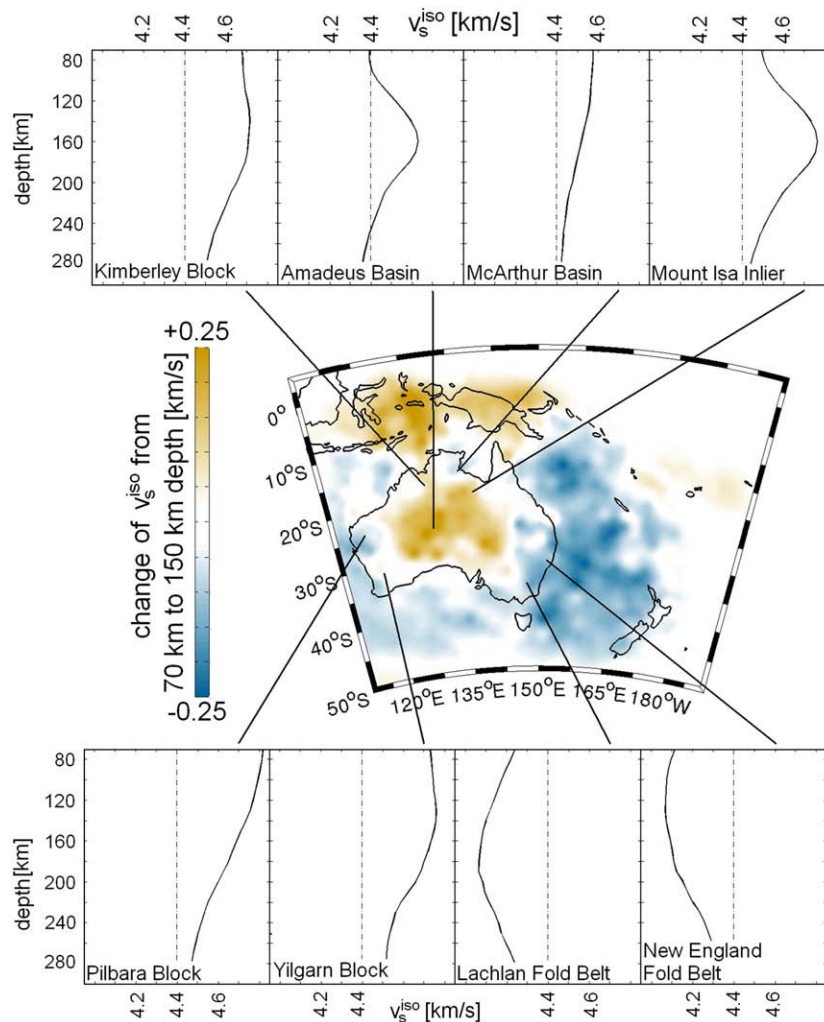


Fig. 7. The central figure shows the change of the isotropic S wave speed, v_s^{iso} from 70 km to 150 km depth. Brownish colours indicate a velocity increase and blue a velocity decrease with increasing depth. A selection of v_s^{iso} profiles for a variety of tectonic regions is plotted above and below the central figure. The velocity increase reaches 0.25 km/s over 80 km depth beneath the Amadeus Basin. (For interpretation of the references to colour in this figure legend, the reader is referred to the web version of this article.)

5.1.4. Micro-continents and hotspot tracks in the Tasman Sea

Above 150 km depth, a north–south trending band of neutral velocities appears beneath the Tasman Sea, in agreement with the results by Fishwick et al. (2008). It approximately follows the micro-continental Lord Howe Rise and the Lord Howe and Tasmanid hotspot tracks (e.g. McDougall and Duncan, 1988; Sutherland, 2003). The neutral-velocity band is thus likely to be related to the comparatively high velocities of continental lithosphere and the extraction of heat by hotspot volcanism. We note, however, that pronounced low-velocity patches are not visible in the vicinity of the present-day locations of the Tasmanid and Lord Howe hotspots (Fig. 6).

A band of neutral to fast velocities also appears beneath the micro-continental Norfolk ridge, linking the North Island of New Zealand to New Caledonia. While neutral velocities above 150 km depth may be explained by the presence of continental lithosphere, the origin of fast velocities below 200 km depth is unknown.

5.1.5. Adelaide rift

We observe lower than average wave speeds localised around the Proterozoic to Early Paleozoic Adelaide rift in South Australia. The low wave speeds coincide with a region of elevated seismicity (Leonard, 2008) and with the South Australian Heat Flow Anomaly, where surface heat flow exceeds the Proterozoic average of $\approx 50 \text{ mWm}^{-2}$ by more than 40 mWm^{-2} . Neumann et al. (2000) argue that the anomalously high heat flow mainly results from the enrichment of U and Th in Proterozoic granites. Our results suggest that locally elevated temperatures in the upper mantle may also contribute to the heat flow anomaly and to the ongoing tectonic activity in the Flinders Ranges (Stewart, 1976).

5.2. Origin and interpretation of radial seismic anisotropy

There are two contributions to observed seismic anisotropy: First, mineralogical seismic anisotropy (MSA) is the result of the coherent lattice-preferred orientation (LPO) of anisotropic minerals over length scales that exceed the resolution length. The LPO of the most abundant and most anisotropic upper-mantle minerals, olivine and pyroxenes, causes both azimuthal and polarisation anisotropy. The radial MSA in the tomographic images is the mineralogical polarisation anisotropy averaged over the azimuths covered in a specific region. Second, structural seismic anisotropy (SSA) is induced by heterogeneities with length scales that can not be resolved. Classical examples are thin layers (e.g. Backus, 1962) and coherently aligned melt pockets (e.g. Mainprice, 1997).

MSA and SSA can not be distinguished seismologically, but the influence of SSA on the tomographic images can be reduced by increasing the tomographic resolution. Both full waveform tomography and the integration of seismic, topographic, gravity and magnetic data (Simons and van der Hilst, 2003; Bokelmann and Wuestefeld, 2009) are important steps in this direction.

The geodynamic interpretation of seismic anisotropy is based on its relation to flow in the Earth. Horizontal (vertical) flow causes preferentially horizontal (vertical) alignment of small-scale heterogeneities and thus leads to positive (negative) radial SSA. The development of MSA in the presence of flow depends mostly on the relation between shear strain and the LPO formation of olivine. Under uppermost mantle conditions and for shear strains exceeding about 50%, the [100] axis of olivine lies nearly parallel to the flow direction (Zhang and Karato, 1995). This causes a $v_{sh} > v_{sv}$ signature, i.e. positive radial anisotropy, for shear waves travelling parallel to the flow plane. SSA and MSA add constructively in this case.

The standard interpretation of positive (negative) radial anisotropy in terms of horizontal (vertical) flow is not justified under conditions where departures from the alignment of the [100] axis in the direction of shear are known to occur. These include pressures above 8 GPa ($\approx 250 \text{ km}$ depth, Mainprice et al., 2005; Raterron et al.,

2009) and large water contents (200 ppm, Jung and Karato, 2001, Katayama et al., 2004). The determination of the precise LPO-MSA relation for the full range of possible mantle conditions is an active area of research. The following interpretations are thus preliminary to some degree.

5.3. Tectonic and mineralogic interpretation of radial anisotropy

Seismic anisotropy in the Australasian region depends strongly on depth, thus reflecting the various geodynamic and mineralogic mechanisms responsible for its formation. In the interest of readability, we proceed with our interpretation from shallower to deeper depth levels:

5.3.1. Seismic anisotropy above 150 km depth

The anisotropy above 150 km depth (Fig. 4) reveals a clear ocean–continent dichotomy: Anisotropy beneath the Coral and Tasman Seas is generally positive, ranging between +3% and +7%. The maximum oceanic rms anisotropy, +6%, occurs around 70 km depth (Fig. 8, left). The location of the oceanic rms peak is thus significantly shallower

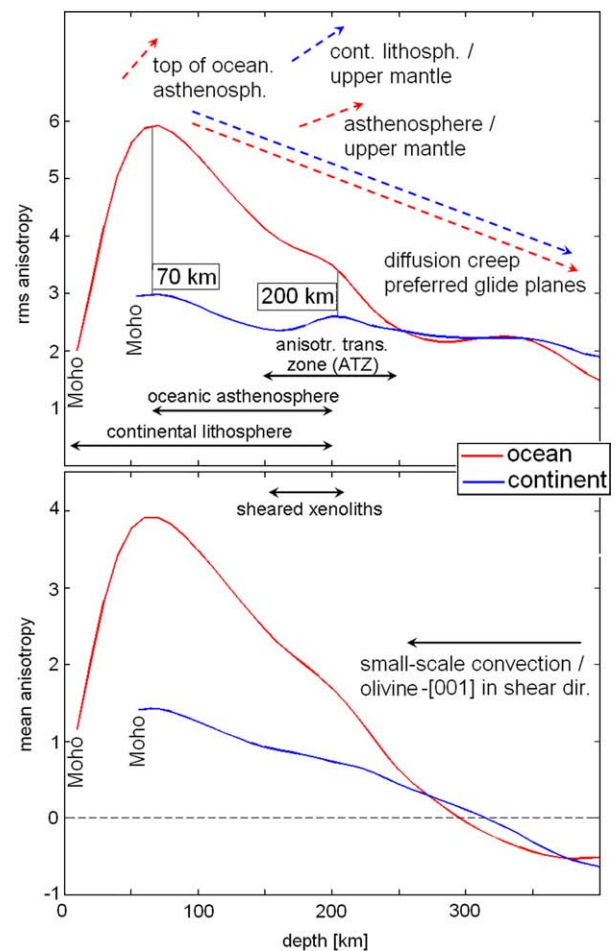


Fig. 8. Horizontal averages of the rms (top) and mean (bottom) radial anisotropy, $(v_{sh} - v_{sv})/v_{sv}^0$ as a function of depth. The averages are over the continental (blue solid curve) and oceanic (red solid curve) regions with non-zero ray coverage. Dashed arrows are qualitative indicators of the different contributions that lead to increasing (upward pointing) or decreasing (downward pointing) anisotropy beneath the continent (blue) and the ocean (red). Black arrows mark the approximate depth intervals of the continental lithosphere, the oceanic asthenosphere, the anisotropic transition zone (ATZ), the region where sheared xenoliths originate, and the region where small-scale convection and the alignment of the olivine [001] axis in the direction of shear are expected. (For interpretation of the references to colour in this figure legend, the reader is referred to the web version of this article.)

than the centre of the asthenospheric low-velocity channel that oscillates around 150 km depth, in accord with previous studies (e.g. Zielhuis and van der Hilst, 1996; Fichtner et al., 2009a). This observation is nevertheless consistent with LPO induced by asthenospheric flow, when the largest shear strains occur at the top and bottom boundaries of a flow channel.

Anisotropy in the rigid continental lithosphere represents past deformation rather than being dynamically supported by present-day flow. It is weaker but more variable than under the Coral and Tasman Seas. We explain the small rms anisotropy (Fig. 8) with the low strain in a stable continent and with the reduced mobility of olivine at temperatures below $\approx 1100^\circ\text{C}$. Strong variations in the anisotropy of the Australian continental lithosphere are supported by SKS splitting studies (Clitheroe and van der Hilst, 1998). The comparatively short spatial wavelengths of continental anisotropy are in agreement with modes of lithospheric deformation where strain localises in narrow regions, as for example during the Paleozoic intraplate orogenies in central Australia (e.g. Sandiford and Hand, 1998). Areas of strong negative radial anisotropy indicate vertically oriented structures, that can, however, hardly be assigned to specific tectonic events.

The rms anisotropy decreases by 30% in the interval from 70–150 km depth. The similarity of this decrease beneath the continent and the adjacent seas leads us to conjecture that it largely results from changes in the preferred olivine glide systems (Mainprice et al., 2005) and/or the increasing contribution of diffusion creep (Karato, 1992).

5.3.2. Anisotropic transition zone between 150 km and 250 km depth

The interval from about 150–250 km depth marks an anisotropic transition zone (ATZ) where the ocean–continent dichotomy is gradually replaced by an anisotropic signature that is similar beneath continental Australia and the Coral and Tasman Seas.

Under the Coral and Tasman Seas the rms anisotropy drops from 5% to 2.5% within the ATZ. Patches of negative anisotropy appear, leading to a reduction of the mean anisotropy from 2% to 0.5% (Fig. 8). Beneath the continent, the rms anisotropy oscillates around 2.7% within the ATZ. It attains a weak maximum at 200 km depth. The mean anisotropy, however, drops from 1% to 0.5%, again indicating that regions with negative anisotropy gain importance. Studies of azimuthal anisotropy (Debayle and Kennett, 2000a,b; Simons et al., 2002) confirm that the general character of anisotropy changes around 150 km depth.

The ATZ, as observed seismologically, is the combined effect of mineralogical, chemical and rheological transitions that are not entirely separable. Around 200 km depth, the depleted and rigid continental lithosphere passes into the fertile and convecting upper mantle. The deformation gradient, i.e. strain, is likely to be responsible for the maximum rms anisotropy that we observe at 200 km depth beneath the continent (Fig. 8). Strongly deformed or “sheared” xenoliths originate from this rheological boundary layer (e.g. James et al., 2004). Our tomographic images indicate that the oceanic asthenosphere terminates in the lower half of the ATZ. Strain in the associated rheological boundary layer is a likely explanation of the slight deflection in the oceanic rms anisotropy curve (Fig. 8) near 200 km depth. The effect is, however, not as pronounced as between the continental lithosphere and the convecting upper mantle.

5.3.3. Anisotropy below 250 depth

Radial anisotropy in AMSAN.19 continues to be present at depths below 250 km, with a horizontally averaged rms value around 3%. No obvious difference between anisotropy beneath the continent and the Coral and Tasman Seas exists. We do not observe a broad region of positive anisotropy under continental Australia that may be expected to result from asthenospheric flow (e.g. Gung et al., 2003). This is in agreement with the absence of a low-velocity layer beneath the continent in AMSAN.19 and previous models (e.g. Debayle and Kennett, 2000a,b; Simons et al., 2002; Fichtner et al., 2009a).

Anisotropy at depths exceeding 250 km has frequently been observed (e.g. Alsina and Snieder, 1995; Trampert and van Heijst, 2002; Panning and Romanowicz, 2006). This is in contrast to the results of Gaherty and Jordan (1995) who found upper-mantle models for Australia where anisotropy is confined to the uppermost 252 ± 5 km. They associated the abrupt disappearance of anisotropy with the Lehmann (1961) discontinuity that Karato (1992) explained with the transition from dislocation to diffusion creep. Our results, however, suggest, that anisotropy below 250 km may only appear to be absent when averaged over too long distances, because deep anisotropy has wavelengths below 500 km. Anisotropy on length scales exceeding 2000 km is below 0.7%. Deep anisotropy as found in AMSAN.19 is consistent with results of recent high-pressure experiments on olivine where dislocation creep continues to be dominant to depth of 330 km (Mainprice et al., 2005; Raterron et al., 2009). The dislocation-to-diffusion creep transition must be sufficiently smooth to locally allow for $>2\%$ rms anisotropy below 250 km depth.

While the rms anisotropy stabilises around 2% in the uppermost mantle, the mean anisotropy drops below 0 near 300 km depth, indicating the prevalence of regions with negative radial anisotropy. There are two plausible contributions to this observation: (1) As demonstrated by Raterron et al. (2009), the dominant slide systems of olivine change near 250 km depth, leading to the alignment of the [001] axis in the shear direction. The resulting radial anisotropy would be negative in the presence of horizontal flow (Mainprice et al., 2005). (2) Small-scale sublithospheric convection (SSC) in the form of localised cold downwellings may provide the strain necessary for LPO formation. SSC develops preferentially along passive continental margins and in regions where the thickness of continental lithosphere varies strongly (e.g. O'Neill et al., 2003). Cold downwellings below 250 km depth tend to align the olivine [001] axis near vertically, thus generating positive radial anisotropy (Mainprice et al., 2005; Raterron et al., 2009). The expected SSC signature – fast velocities in conjunction with positive anisotropy near a continent boundary – can be found along the north-western continental margin of Australia. We note, however, that this interpretation should be considered preliminary because lateral resolution below 300 km depth is limited.

6. Conclusions

We have developed and successfully applied the first continental-scale full waveform tomography for radially anisotropic upper-mantle structure. The principal advantages of our approach are the accurate simulation of elastic wave propagation through realistic 3D models, the extraction of full waveform information, the iterative improvement of the Earth model and the absence of crustal corrections.

We conjecture that long-wavelength discrepancies between images of radial anisotropy are mostly due to methodological differences. This becomes most apparent in the dependence of radial anisotropy on the number of iterations. With an increasing number of iterations, apparent anisotropy can be explained increasingly well by isotropic structure. Linearised inversions may therefore overestimate anisotropy. More research on this topic is certainly required.

Our model reveals neutral to low-velocity patches beneath central Australia, possibly related to localised intraplate deformation. Increasing seismic velocities between the Moho and 150 km depth indicate thermochemical variations caused by the formation and fragmentation of a Centralian Superbasin. Radial anisotropy above 150 km depth reveals a clear ocean–continent dichotomy, with strong $v_{sh} > v_{sv}$ beneath the Coral and Tasman Seas and a more variable and weaker anisotropy beneath continental Australia. The dichotomy disappears between 150–250 km depth, where the continental lithosphere and the oceanic asthenosphere pass into the convecting mantle. Significant anisotropy persists below 250 km depth. It is consistent with sublithospheric small-scale convection and a change in the dominant glide system of olivine. More quantitative

interpretations of the tomographic models depend on progress made in the geodynamic modelling of seismic observables (Becker et al., 2008; Schubert et al., 2009a,b).

7. Uncited references

Debayle et al., 2005

Acknowledgements

We are particularly grateful to Rocco Malservisi, Jean-Paul Montagner and Eric Debayle for discussions that helped us to improve the manuscript. We would also like to thank the Alexander von Humboldt Foundation, the German Academic Exchange Service (DAAD) and the Bavarian Elite Network (ENB) for their support. The data used in this study were provided by Iris, GEOSCOPE, Geoscience Australia and the temporary networks operated by the Research School of Earth Sciences at the Australian National University. We thank Armando Arcidiaco, Agus Abdullah, Stewart Fishwick and Hrvoje Tkalčić for their help with the temporary network data and the station responses. The high-performance computations for the solution of the waveform tomographic problem would not have been possible without the support of the Leibniz Rechenzentrum in Garching. Many thanks also to Jens Oeser for creating a unique computing infrastructure at the Institute of Geophysics at Munich University.

Appendix A. Supplementary Data

Supplementary data associated with this article can be found, in the online version, at doi:10.1016/j.epsl.2009.12.003.

References

- Abdulah, A., 2007. Seismic body wave attenuation tomography beneath the Australasian region. PhD Thesis, The Australian National University.
- Alsina, D., Snieder, R., 1995. Small-scale sublithospheric continental mantle deformation: constraints from SKS splitting observations. *Geophys. J. Int.* 123, 431–448.
- Backus, G.E., 1962. Long-wave elastic anisotropy produced by horizontal layering. *J. Geophys. Res.* 67, 4427–4440.
- Bassin, C., Laske, G., Masters, G., 2000. The current limits of resolution for surface wave tomography in North America. *Eos Transactions AGU* 81, Fall Meeting Supplement F897.
- Becker, T.W., Kustowski, B., Ekström, G., 2008. Radial anisotropy as a constraint for upper mantle rheology. *Earth Planet. Sci. Lett.* 267, 213–227.
- Bokelmann, G.H.R., Wuestefeld, A., 2009. Comparing crustal and mantle fabric from the North American craton using magnetics and seismic anisotropy. *Earth Planet. Sci. Lett.* 277, 355–364.
- Bozdağ, E., Trampert, J., 2008. On crustal corrections in surface wave tomography. *Geophys. J. Int.* 172, 1066–1082.
- Cammarano, F., Goes, S., Vacher, P., Giardini, D., 2003. Inferring upper-mantle temperatures from seismic velocities. *Phys. Earth Planet. Int.* 138, 197–222.
- Clitheroe, G., van der Hilst, R.D., 1998. Complex anisotropy in the Australian lithosphere from shear wave splitting in broad-band SKS records. *Structure and Evolution of the Australian Continent: AGU Geodynamics Series*, vol. 26, pp. 73–87.
- Cull, J.P., Conley, D., 1983. Geothermal gradients and heat flow in Australian sedimentary basins. *J. Aust. Geol. Geophys.* 8, 329–337.
- Debayle, E., Kennett, B.L.N., 2000a. The Australian continental upper mantle: structure and deformation inferred from surface waves. *J. Geophys. Res.* 105, 25423–25450.
- Debayle, E., Kennett, B.L.N., 2000b. Anisotropy in the Australasian upper mantle from Love and Rayleigh waveform inversion. *Earth Planet. Sci. Lett.* 184, 339–351.
- Debayle, E., Kennett, B.L.N., Priestley, K., 2005. Global azimuthal seismic anisotropy and the unique plate-motion deformation of Australia. *Nature* 433, 509–512.
- Dumbser, M., Käser, M., 2006. An arbitrary high order discontinuous Galerkin method for elastic waves on unstructured meshes II: The three-dimensional isotropic case. *Geophys. J. Int.* 167, 319–336.
- Dziewonski, A.M., Anderson, D.L., 1981. Preliminary reference Earth model. *Phys. Earth Planet. Int.* 25, 297–356.
- Faccioli, E., Maggio, F., Paolucci, R., Quarteroni, A., 1997. 2D and 3D elastic wave propagation by a pseudo-spectral domain decomposition method. *J. Seismol.* 1, 237–251.
- Fichtner, A., Igel, H., 2008. Efficient numerical surface wave propagation through the optimization of discrete crustal models – a technique based on non-linear dispersion curve matching (DCM). *Geophys. J. Int.* 173, 519–533.
- Fichtner, A., Bunge, H.-P., Igel, H., 2006. The adjoint method in seismology – I Theory. *Phys. Earth Planet. Int.* 157, 86–104.
- Fichtner, A., Kennett, B.L.N., Igel, H., Bunge, H.-P., 2008. Theoretical background for continental and global scale full-waveform inversion in the time–frequency domain. *Geophys. J. Int.* 175, 665–685.
- Fichtner, A., Kennett, B.L.N., Igel, H., Bunge, H.-P., 2009a. Spectral-element simulation and inversion of seismic waves in a spherical section of the Earth. *J. Numer. Anal. Ind. Appl. Math.* 4, 11–22.
- Fichtner, A., Kennett, B.L.N., Igel, H., Bunge, H.-P., 2009b. Full seismic waveform tomography for upper-mantle structure in the Australasian region using adjoint methods. *Geophysical Journal International* 179, 1703–1725.
- Fishwick, S., Reading, A.M., 2008. Anomalous lithosphere beneath the Proterozoic of western and central Australia: a record of continental collision and intraplate deformation? *Precambrian Res.* 166, 111–121.
- Fishwick, S., Kennett, B.L.N., Reading, A.M., 2005. Contrasts in lithospheric structure within the Australian craton – insights from surface wave tomography. *Earth Planet. Sci. Lett.* 231, 163–176.
- Fishwick, S., Heintz, M., Kennett, B.L.N., Reading, A.M., Yoshizawa, K., 2008. Steps in lithospheric thickness within eastern Australia, evidence from surface wave tomography. *Tectonics* 27. doi:10.1029/2007TC002116.
- Gaherty, J.B., Jordan, T.H., 1995. Lehmann discontinuity as the base of an anisotropic layer beneath continents. *Science* 268, 1468–1471.
- Goes, S., Simons, F.J., Yoshizawa, K., 2005. Seismic constraints on temperature of the Australian uppermost mantle. *Earth Planet. Sci. Lett.* 236, 227–237.
- Hales, A.L., 1969. A seismic discontinuity in the lithosphere. *Earth. Planet. Sci. Lett.* 7, 44–46.
- James, D.E., Boyd, F.R., Schutt, D., Bell, D.R., Carlson, R.W., 2004. Xenolith constraints on seismic velocities in the upper mantle beneath southern Africa. *Geochem. Geophys. Geosyst.* 5, Q01002. doi:10.1029/2003GC000551.
- Jaques, A.L., O'Neill, H.S.C., Smith, C.B., Moon, J., Chappell, B.W., 1990. Diamondiferous peridotite xenoliths from the Argyle (AK1) lamproite pipe, Western Australia. *Contrib. Mineral. Petrol.* 104, 255–276.
- Jung, H., Karato, S.-I., 2001. Water-induced fabric transitions in olivine. *Science* 293, 1460–1463.
- Kaiho, Y., Kennett, B.L.N., 2000. Three-dimensional structure beneath the Australasian region from refracted wave observations. *Geophys. J. Int.* 142, 651–668.
- Karato, S.-I., 1992. On the Lehmann discontinuity. *Geophys. Res. Lett.* 19, 2255–2258.
- Katayama, I., Jung, H., Karato, S.-I., 2004. New type of olivine fabric from deformation experiments at modest water content and low stress. *Geology* 32, 1045–1048.
- Kennett, B.L.N., Engdahl, E.R., Buland, R., 1995. Constraints on seismic velocities in the Earth from travel times. *Geophys. J. Int.* 122, 108–124.
- Klemme, S., 2004. The influence of Cr on the garnet-spinel transition in the Earth's mantle: experiments in the system MgO–Cr₂O₃–SiO₂ and thermodynamic modelling. *Lithos* 77, 639–646.
- Komatitsch, D., Tromp, J., 2002. Spectral-element simulations of global seismic wave propagation – I Validation. *Geophys. J. Int.* 149, 390–412.
- Konishi, K., Kawai, K., Geller, R.J., Fuji, N., 2009. MORB in the lowermost mantle beneath the western Pacific: evidence from waveform inversion. *Earth Planet. Sci. Lett.* 278, 219–225.
- Lebedev, S., Boonen, J., Trampert, J., 2009. Seismic structure of Precambrian lithosphere: new constraints from broad-band surface-wave dispersion. *Lithos* 109, 96–111.
- Lehmann, I., 1961. S and the structure of the upper mantle. *Geophys. J. Roy. Astron. Soc.* 4, 124–138.
- Leonard, M., 2008. One hundred years of earthquake recording in Australia. *Bull. Seismol. Soc. Am.* 98, 1458–1470.
- Levshin, A.L., Schweitzer, J., Weidle, C., Shapiro, N.M., Ritzwoller, M.H., 2007. Surface wave tomography of the Barents Sea and surrounding regions. *Geophys. J. Int.* 170, 441–459.
- Mainprice, D., 1997. Modelling the anisotropic seismic properties of partially molten rocks found at mid-ocean ridges. *Tectonophysics* 279, 161–179.
- Mainprice, D., Tommasi, A., Couvy, H., Cordier, P., Frost, D.J., 2005. Pressure sensitivity of olivine slip systems and seismic anisotropy of Earth's upper mantle. *Nature* 433, 731–733.
- McDougall, I., Duncan, R.A., 1988. Age progressive volcanism in the Tasmanid Seamounts. *Earth Planet. Sci. Lett.* 89, 207–220.
- Montagner, J.-P., 2002. Upper mantle low anisotropy channels below the Pacific Plate. *Earth Planet. Sci. Lett.* 202, 263–274.
- Myers, J.S., Shaw, R.D., Tyler, I.M., 1996. Tectonic evolution of Proterozoic Australia. *Tectonics* 15, 1431–1446.
- Nataf, H.C., Ricard, Y., 1995. 3SMAC: an a priori tomographic model of the upper mantle based on geophysical modeling. *Phys. Earth Planet. Int.* 95, 101–122.
- Nettel, M., Dziewonski, A.M., 2008. Radially anisotropic shear velocity structure of the upper mantle globally and beneath North America. *J. Geophys. Res.* 113, B02303. doi:10.1029/2006JB004819.
- Neumann, N., Sandiford, M., Foden, J., 2000. Regional geochemistry and continental heat flow: implications for the origin of the South Australian heat flow anomaly. *Earth Planet. Sci. Lett.* 183, 107–120.
- O'Neill, C., Moresi, L., Lenardic, A., Cooper, C.M., 2003. Inferences on Australia's heat flow and thermal structure from mantle convection modelling results: Geological Society of Australia, Special Publication, vol. 22, pp. 169–184.
- Oeser, J., Bunge, H.-P., Mohr, M., 2006. Cluster design in the Earth sciences: tethys. *High Perform. Comput. Commun. Proc.* 4208, 31–40.
- Panning, M., Romanowicz, B., 2006. A three-dimensional radially anisotropic model of shear velocity in the whole mantle. *Geophys. J. Int.* 167, 361–379.
- Paulsen, H., 1987. Lateral heterogeneity of Europe's upper mantle as inferred from modelling of broad-band body waves. *Geophys. J. Roy. Astron. Soc.* 91, 171–199.
- Peter, D., Boschi, L., Woodhouse, J., 2009. Tomographic resolution of ray and finite-frequency methods: a membrane-wave investigation. *Geophys. J. Int.* 177, 624–638.

- Raterron, P., Amiguet, E., Chen, J., Li, L., Cordier, P., 2009. Experimental deformation of olivine single crystals at mantle pressures and temperatures. *Phys. Earth Planet. Int.* 172, 74–83.
- Sandiford, M., Hand, M., 1998. Controls on the locus of intraplate deformation in central Australia. *Earth Planet. Sci. Lett.* 162, 97–110.
- Schuberth, B.S.A., Bunge, H.-P., Steinle-Neumann, G., Moder, C., Oeser, J., 2009a. Thermal versus elastic heterogeneity in high-resolution mantle circulation models with pyrolite composition: High plume excess temperatures in the lowermost mantle. *Geochem. Geophys. Geosyst.* 10, Q01W01. doi:10.1029/2008GC002235.
- Schuberth, B.S.A., Bunge, H.-P., Ritsema, J., 2009b. Tomographic filtering of high-resolution mantle circulation models: can seismic heterogeneity be explained by temperature alone? *Geochem. Geophys. Geosyst.* 10, Q05W03. doi:10.1029/2009GC002401.
- Sieminski, A., Liu, Q., Trampert, J., Tromp, J., 2007a. Finite-frequency sensitivity of surface waves to anisotropy based upon adjoint methods. *Geophys. J. Int.* 168, 1153–1174.
- Sieminski, A., Liu, Q., Trampert, J., Tromp, J., 2007b. Finite-frequency sensitivity of body waves to anisotropy based upon adjoint methods. *Geophys. J. Int.* 171, 368–389.
- Simons, F.J., van der Hilst, R.D., 2003. Seismic and mechanical anisotropy and the past and present deformation of the Australian lithosphere. *Earth Planet. Sci. Lett.* 211, 271–286.
- Simons, F.J., Zielhuis, A., van der Hilst, R.D., 1999. The deep structure of the Australian continent from surface wave tomography. *Lithos* 48, 17–43.
- Simons, F.J., van der Hilst, R.D., Montagner, J.-P., Zielhuis, A., 2002. Multimode Rayleigh wave inversion for heterogeneity and azimuthal anisotropy of the Australian upper mantle. *Geophys. J. Int.* 151, 738–754.
- Stewart, I.C.F., 1976. Fractures and movement of the Adelaide rift zone. *Science* 264, 198–199.
- Sutherland, F.L., 2003. Boomerang migratory intraplate Cenozoic volcanism, eastern Australian rift margins and the Indian–Pacific mantle boundary: Geological Society of Australia, Special Publication, vol. 22, pp. 203–221.
- Takeuchi, H., Saito, M., 1972. Seismic surface waves. *Methods in Computational Physics* 11. Academic Press, New York, pp. 217–295.
- Tape, C., Liu, Q., Maggi, A., Tromp, J., 2009. Adjoint tomography of the southern California crust. *Science* 325, 988–992.
- Tarantola, A., 1988. Theoretical background for the inversion of seismic waveforms, including elasticity and attenuation. *Pure Appl. Geophys.* 128, 365–399.
- Tian, Y., Sigloch, K., Nolet, G., 2009. Multiple-frequency SH-wave tomography of the western US upper mantle. *Geophys. J. Int.* 178, 1384–1402.
- Trampert, J., van Heijst, H.J., 2002. Global azimuthal anisotropy in the transition zone. *Science* 296, 1297–1299.
- Tromp, J., Tape, C., Lui, Q., 2005. Seismic tomography, adjoint methods, time reversal and banana–doughnut kernels. *Geophys. J. Int.* 160, 195–216.
- Yoshizawa, K., Kennett, B.L.N., 2004. Multimode surface wave tomography for the Australian region using a three-stage approach incorporating finite frequency effects. *J. Geophys. Res.* 109. doi:10.1029/2002JB002254.
- Zhang, S., Karato, S.-I., 1995. Lattice preferred orientation of olivine aggregates deformed in simple shear. *Nature* 375, 774–777.
- Zielhuis, A., van der Hilst, R.D., 1996. Upper-mantle shear velocity beneath eastern Australia from inversion of waveforms from SKIPPY portable arrays. *Geophys. J. Int.* 127, 1–16.